Detecting Source Regions of Wave Activities in the Tropical Atmosphere by Applying Beamforming to Interpolated Data Grids

QI HU AND ZHAONING LIANG

School of Natural Resources, and Department of Geosciences, University of Nebraska at Lincoln, Lincoln, Nebraska

MICHAEL W. HOFFMAN

Department of Electrical Engineering, University of Nebraska at Lincoln, Lincoln, Nebraska

(Manuscript received 6 February 2008, in final form 15 July 2008)

ABSTRACT

Wave activities are primary sources of weather disturbances and cyclones in the tropical atmosphere. One such activity is the intraseasonal variations in wind, convection, and precipitation in the tropical Indian and western tropical Pacific region. These variations affect the intensity, break and reset, and rainfall in the Indian and the East Asian monsoons. Detecting the source regions of these wave activities is essential for understanding and for prediction of wave development. In this study, a fixed beamforming method is proposed to deduce source regions of some wave activities in the tropical atmosphere. This method is tested with simulations of single and distributed complex sources of waves and, then, fixed beamformers are applied to the ECMWF interpolated data grids to detect and identify source regions of the intraseasonal oscillations–waves in the tropical Indian and tropical Pacific Ocean region. Results show that the fixed beamforming technique can uniquely identify the source regions of the intraseasonal oscillations. Applications of this method have revealed various source regions of all major intraseasonal oscillation (ISO) events in the tropical Indian and western equatorial Pacific region during the 29 yr from 1974 to 2002. Knowing these source regions will make it possible to extract the relevant information and, thus, to better understand the development of the intraseasonal oscillations as well as their effects on the tropical weather and climate.

1. Introduction

In the tropical atmosphere, wave activities are primary sources of weather disturbances and cyclones. For instance, the intraseasonal variations in wind, convection, and precipitation in the tropical Indian and western Pacific Ocean region (Madden and Julian 1971, 1972) evolve from wave activities. These variations affect the Indian summer monsoon activities (e.g., monsoon intensity, break, and reset; Yasunari 1979; Lau and Chen 1986), as well as the East Asian monsoon rainfall (e.g., Wang and Ho 2002). In the Atlantic region, the tropical easterly waves emerging from convection over land in tropical Africa sometimes develop into hurricanes in the tropical Atlantic in boreal autumn, influencing Central and North America (Landsea and Gray 1992). Because these tropical waves often develop into severe weather systems and have directly affected the monsoon circulations in the extratropics and midlatitudes, identifying source regions of these waves, where they originate, would be helpful for monitoring, understanding, and predicting hurricanes and monsoon variations. Moreover, in the case of the intraseasonal variations in the tropical Pacific, knowing the source regions of the intraseasonal waves would allow us to analyze the specific physical environment in the source regions and examine processes that have initiated and sustained the intraseasonal variations.

In this study, we propose a method using fixed beamformers on interpolated data grids to achieve this goal of deducing source regions of intraseasonal waves in the tropical atmosphere from observational data. Beamforming has been used since the 1960s–70s. Adaptive beamformers using a spaced array of sensors

Corresponding author address: Dr. Qi Hu, University of Nebraska at Lincoln, 707 Hardin Hall, Lincoln, NE 68583-0987.
E-mail: qhu2@unl.edu

DOI: 10.1175/2008JTECHA1121.1

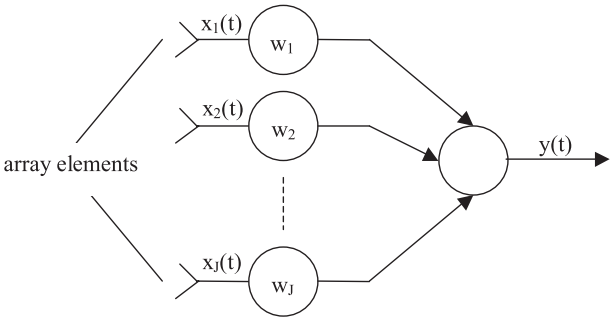

FIG. 1. Signal processing regime of a fixed beamformer (adapted from van Veen and Buckley 1988). In the diagram, $x_j(t)$ is the signal "captured" by the jth sensor of the beamformer, J is the number of sensors in the beamformer, $t = 1, 2...N$ is the time series of the signal being captured, w_j, $j = 1, 2...J$ form the weight vectors of each sensor, multiplied as a complex conjugate, and $y(t)$ is the synthesized signal by all the sensors [see Eq. (1) in text].

have been developed and applied extensively in detection of sources of seismic signals (e.g., Lacoss 1968). Application of beamformers to atmospheric waves and variations has however only been made in a retrieval of high-accuracy wind profile from atmospheric Doppler radars with arrays of receivers (Cheong et al. 2004). This study extends applications of the fixed beamformers to tropical intraseasonal waves and oscillations. Because the atmospheric data are gathered, processed, and then stored in regular and interpolated grids, this particular data structure allows us to use arrays of data grid points as sensor arrays for the fixed beamformer. This perspective is also a key contribution of this research to beamforming techniques.

Because beamforming has only been used for a few applications in atmospheric studies it is necessary to describe this method and specifics for its applications for detecting source regions of waves in the tropical atmosphere. After describing the fixed beamforming method in the next section (section 2) we will test and evaluate the method using single and complex distributed wave sources of known properties. Results of these tests will show the capacity of the fixed beamforming technique to deduce source regions of waves. In section 3, the tested method will be applied to detecting the source regions of the tropical intraseasonal oscillations (ISOs) and waves. In this application, the data arrays of both the 850-hPa zonal winds and the outgoing longwave radiation (OLR) in the tropical Indian and Pacific Oceans were used as sensor arrays for the fixed beamformer. Results, which also are detailed in section 3, show that the fixed beamforming technique can uniquely detect the source regions of ISO observed in the tropical Indian and Pacific Ocean region. Conclusions of this study are in section 4.

2. Fixed beamformer

a. Theory

A beamformer is a processor providing a versatile form of spatial filtering (van Veen and Buckley 1988). It contains an array of sensors that collect signals of propagating waves (in terms of, e.g., their reflection in wind anomalies) and can be used to determine the source regions of a specific signal or signals of certain frequency bands. The "fixed beamformer" is a data-independent and robust beamformer (van Veen and Buckley 1988). It performs spatial filtering by separating signals that have overlapping frequencies but are generated at different sources. This capacity of the method is particularly important to detect source regions of intraseasonal waves in the tropical region because these waves are often generated by sources of somewhat different frequencies.

The spatial filtering process of fixed beamforming is illustrated in Fig. 1. A spatial signal, $x(t)$, where t is the time index, consisting of different frequency waves generated by sources at different locations, is captured by one of the sensors in the array. These sensors are the components of the fixed beamformer. Because they are placed at different locations they will capture the signals at slightly different times, depending on the signals' traveling speed and source location. For example, sensors closer to a source would receive the signal earlier than the sensors farther away from the source. From the differentials of such lags in time among the sensors when they receive a specific signal, the direction of the source releasing this signal at a specified frequency, or a band of it, can be identified. This process can be performed after moving the array of sensors to different locations and "tracing" and eventually "pinning" the particular source region of the waves–signals (van Veen and Buckley 1988).

The output of the fixed beamformer at time t is a linear combination of the data collected by the sensors at t,

$$y(t) = \mathbf{W}^H \mathbf{X}(t), \tag{1}$$

where $\mathbf{W} = \{w_1, w_2, w_3, \ldots, w_J\}^{\mathrm{T}}$ is the weight vector, H represents Hermitian (complex conjugate) transpose, $\mathbf{X}(t) = \{x_1(t), x_2(t), x_3(t), \ldots x_J(t)\}^{\mathrm{T}}$ is the data series from the sensor array, the superscript T represents transpose, and J is the number of sensors in the beamformer. In a fixed beamformer, the weights $\mathbf{W}$ are fixed or constant, given that we are looking at a particular direction. In adaptive beamforming these weights vary with the input data. Our application exclusively uses fixed, or non-data-adaptive, beamforming. It is conventional in beamforming that we multiply the data, $\mathbf{X}(t)$, by

conjugates of the weights, $\mathbf{W}^H$, so as to simplify notation. It is noted that "the data and weights are complex since in many applications a quadrature receiver is used at each sensor to generate in phase and quadrature data" (van Veen and Buckley 1988).

For observed data $x(t)$ of real numbers, a Hilbert Transform can be applied to generate the complex or analytic data to use in (1). This generation of the analytic signal takes the following three steps (Marple 1999):

1) Apply the discrete-time Fourier transform (DTFT) to the data series:

$$x(k) = \sum_{t=1}^{N} x(t) e^{(-i2\pi)(t-1)(k-1)/N}, \tag{2}$$

where $x(t)$ is the data sequence, k is the frequency index, $k = 1, 2, \ldots N$, N is the total number of time samples, and $i = \sqrt{-1}$.

2) Apply an N-point one-sided discrete-time signal transform:

$$z(k) = \begin{cases} x(1) & \text{for} \quad k = 1 \\ 2x(k) & \text{for} \quad 2 \le k \le N/2 \\ x(N/2+1) & \text{for} \quad k = N/2+1 \\ 0 & \text{for} \quad N/2+2 \le k \le N \end{cases}. \tag{3}$$

This step is necessary to limit the signal frequency to be larger than zero (i.e., resulting in signals with a one-sided spectrum).

3) Apply the inverse DTFT (IDTFT):

$$x^c(t) = \frac{1}{N} \sum_{k=1}^{N} z(k) e^{(i2\pi)(t-1)(k-1)/N}. \tag{4}$$

After this step, the analytic (complex) data series, $x^c(t)$, $t = 1, 2, \ldots, N$, has been generated from the original real observation, $x(t)$, and can be used in (1).

b. Weight vector design

One essential part in constructing the fixed beamformer is designing the weight vector $\mathbf{W}$ in (1). Typically, the elements of $\mathbf{W}$ are designed to create constructive interference at a particular angle. For plane wave signals, weight vector $\mathbf{W}$ has the form

$$\mathbf{W} = [e^{i\Lambda\cdot\mathbf{D}_1}, e^{i\Lambda\cdot\mathbf{D}_2}, \ldots, e^{i\Lambda\cdot\mathbf{D}_J}]^{\mathrm{T}}, \tag{5}$$

where, $\mathbf{\Lambda} = (2\pi/\lambda)(\mathbf{l}\cos\varphi, \mathbf{m}\sin\varphi)$ in which λ is the wavelength of the signal of interest, $\mathbf{D}_k (k = 1, 2, \ldots, J)$ are the position vectors, $(x\mathbf{l} + y\mathbf{m})$, between the coordinate origin and the kth sensor (receiver) of the fixed beamformer, and φ is the arrival angle of the signal of interest (Fig. 2). In describing the position, $\mathbf{l}$ is the unit vector in the east–west direction and $\mathbf{m}$ the unit vector in the north–south direction.

In this study, a two-dimensional fixed beamformer with an array of 3 by 3 sensors is designed to detect source regions of the tropical intraseasonal oscillations in individual ISO events. Figure 2 shows the structure of this fixed beamformer. The distance between any two adjacent sensors is the same and denoted as Δx, and $\Delta x = \Delta y$. To determine D_k in (5) and the weights of the beamformer, we make the sensor at the center of the 3 by 3 array the anchor point (i.e., the origin), and specify its position as $(\mathbf{l},\mathbf{m})$. Accordingly, the position of the neighboring sensors can be specified relative to this origin as shown in Fig. 2. Relative to the time when sensor $(\mathbf{l},\mathbf{m})$ receives the desired signal there will be time differences, either advanced or lagged, between times when the neighboring sensors receive the same signal. Referring to Fig. 2, we can define these differences by (note that the position vector in the previous $\mathbf{D}_k$ now takes the component form of $\mathbf{D}_{l,m}$)

$$\mathbf{D}_{l,m} = \Delta x[\mathbf{l}(-l), \mathbf{m}(-m)] \quad l, m = -1, 0, 1. \tag{6}$$

Applying (6) to (5), we obtain the weight vector, as a function of angle φ, of this two-dimensional 9-sensor fixed beamformer:

$$\mathbf{W} = \begin{bmatrix} e^{i\Lambda\cdot\mathbf{D}_1} \\ e^{i\Lambda\cdot\mathbf{D}_2} \\ \cdot \\ \cdot \\ \cdot \\ e^{i\Lambda\cdot\mathbf{D}_9} \end{bmatrix} = \begin{bmatrix} \exp\{\frac{i2\pi\Delta x}{\lambda}[(-1)\cos\varphi + (-1)\sin\varphi]\} \\ \exp\{\frac{i2\pi\Delta x}{\lambda}[(-1)\cos\varphi + (0)\sin\varphi]\} \\ \\ \\ \exp\{\frac{i2\pi\Delta x}{\lambda}[(+1)\cos\varphi + (+1)\sin\varphi]\} \end{bmatrix}. \tag{7}$$

Substituting (7) and (4) into (1), we get $y(t)$ at each sensor for a wave coming from any specific direction, φ [for that matter we may rewrite $y(t)$ as $y(\varphi,t)$]. By sweeping the weights around 360° (i.e., changing φ from 0° to 360° with a 5° increment, say), we can get 72 different $y(\varphi,t)$ at each sensor at each time. Using the power square root equation,

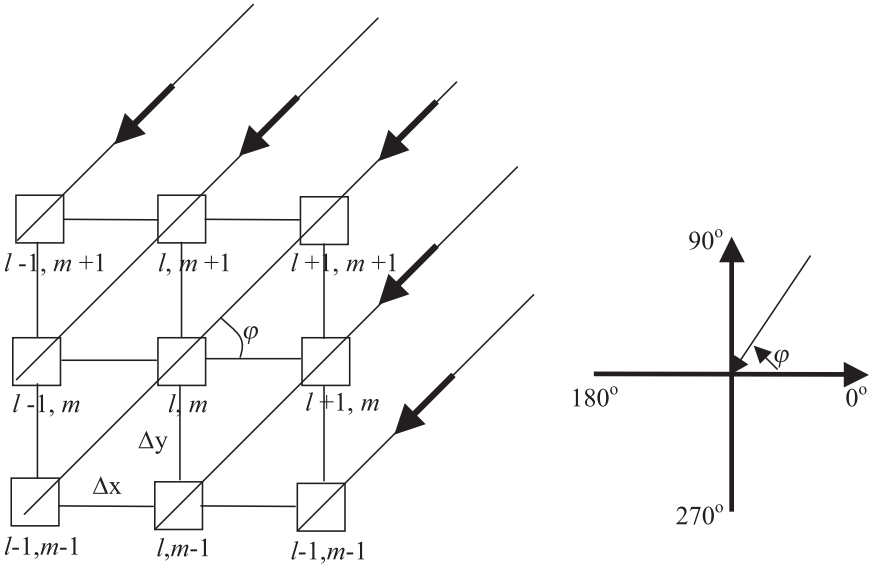

FIG. 2. (left) A schematic of a 2D 3 × 3 (9) sensor fixed beamformer structure. In the beamformer, the distance between adjacent sensors is the same ($\Delta x = \Delta y$). The position of the center sensor, the origin of the array, is (l,m), and the positions of the neighboring sensors in the array are defined according to their spatial relationship with the origin. Arrows show the signal coming azimuth φ, which varies (right) from 0° to 360°.

$$p(\varphi) = \sqrt{\left(\frac{1}{N}\right)\sum_{t=1}^{N}\left|y(\varphi,t)\right|^2}, \tag{8}$$

we can obtain 72 different $p(\varphi)$ for desired signals coming from 0° to 360° around the center of the sensor array. The value of $p(\varphi)$ will be largest only when φ is at the angle that represents the best ''phase delay'' between the signal of interest and the sensors.

By moving the fixed beamformer through atmospheric data grids in the study domain we will obtain estimates of the arrival direction of the dominant signal at every grid point. Then by calculating the divergence of the signal across the study domain we can detect the source location(s) of the desired wave signal. Regions and areas of large divergence are the source regions of the waves.

3. Tests and applications of the fixed beamformer

a. Tests of the fixed beamformer

To examine the applicability of the fixed beamforming technique described in the previous section to deduce wave sources in the tropical atmosphere we used it to first detect known wave sources generated by a simple device,

$$q(x,t) = Ae^{i(sx-\omega t)}. \tag{9}$$

This is a generic solution of wave equation with an initial forcing. In (9), s is the wavenumber, ω is frequency of the waves, and A is the amplitude that is determined by the initial forcing. In this test, these parameters are determined based on studies of mesoscale gravity waves of Zhang (2003) and Wang and Zhang (2007), and take the values of $s = \pi/144$, $\omega = \pi/2$ (h^{-1}), and $A = 10$ hPa. With these values we apply (9) to a grid of 200 × 200 grid points with equal spacing of 10 km between neighboring grid points in the north–south and the east–west directions. The initial wave source is placed at various locations in the grid domain. After waves are generated the beamformer is applied to detect the source region of the waves. Detected source regions are then compared to the actual source locations.

Results of these tests are presented in Figs. 3a and 3b, clearly showing that the fixed beamformer has captured the different single source areas where the wave is released. These test results assure that the designed fixed beamformer can deduce source regions of waves in the atmosphere when data resolution is adequate.

Because the purpose of this beamformer is to detect the source regions of tropical ISO, which result from atmospheric convection (Madden and Julian 1972) that can have varying frequencies from multiple convective bodies clustered together or close to each other, an additional test is designed to further evaluate this method

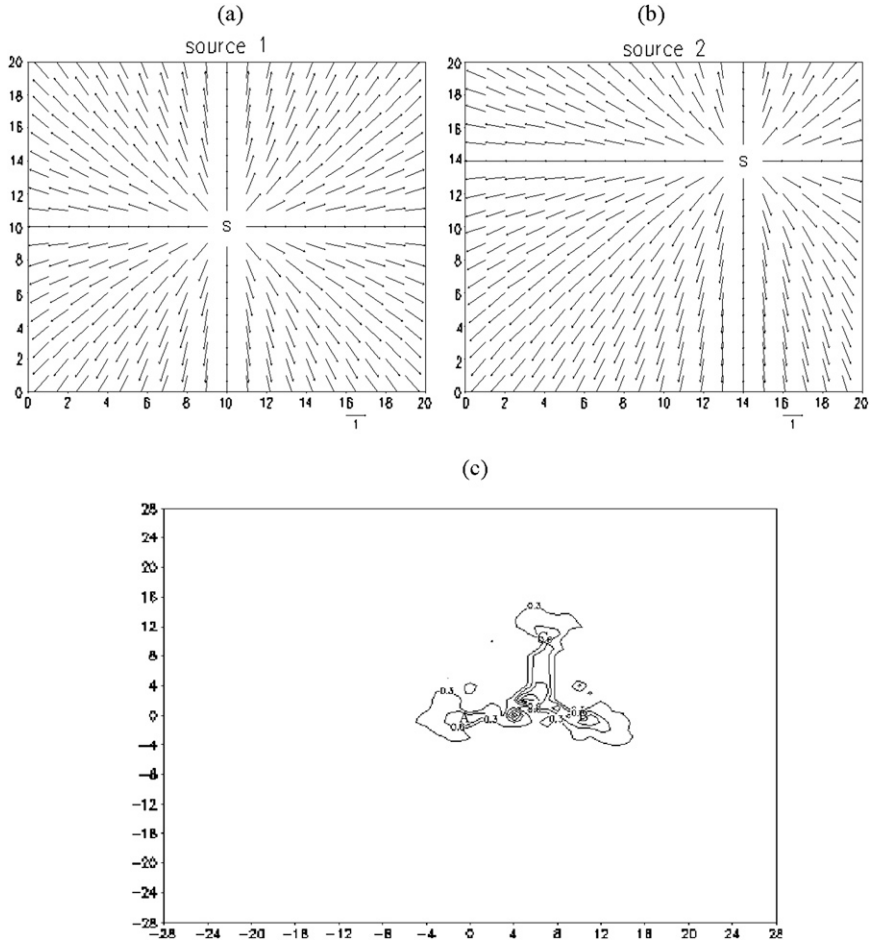

FIG. 3. (a),(b) Test results of the fixed beamformer with a simple wave source at the point marked by "s": (a) source 1 and (b) source 2. (c) Divergence data are plotted for a complex distributed wave source located at $A = \{0,0\}$, $B = \{10,0\}$, and $C = \{7,10\}$ (see text for details).

for its capacity to locate such multiple sources of variations. In this test, a complex and distributed source of waves of slightly different frequencies is placed over a triangular shape, which would roughly mimic the forcing of the coupled Rossby–Kelvin wave shape of the Madden–Julian oscillation in the tropical atmosphere (this particular wave type has been suggested to constitute large portions of the ISO). Specifically, the three wave sources are set at grid points $A = \{0,0\}$, $B = \{10,0\}$, and $C = \{7,10\}$ in the domain of 60 × 60 grid points of 100-km equal gridpoint spacing (Fig. 3c). The source point A releases a wave of frequency $f_A = 2\pi/4$ h, source point B releases a wave of frequency $f_B = f_A + \Delta f$, and source C releases a wave of frequency $f_C = f_A - \Delta f$, and $\Delta f = 0.01f_A, 0.02f_A, \ldots, 0.05f_A$. Waves from these sources have phase speeds of 20 m s^{-1} and amplitude 1. In addition, random noise is added to each wave source to include the effects of random processes that may interfere with the major wave (this mimics the fact that the atmospheric wave measurements are usually generated in the presence of noise or waves of different frequencies or origins). The additive white noise is generated randomly by a pseudorandom noise generator, and its signal is described by Re(noise) = σRe(random noise) and Im(noise) = σIm(random noise), where Re and Im are real and imaginary parts of the complex random noise and σ^2 is the variance. Both Re(noise) and Im(noise) have normal distributions of zero mean and variance σ^2. The intensity of the noise is controlled by the signal-to-noise ratio, SNR = P_s/P_n, where P_s is the power from the signal of the waves and P_n is the power from the signal of the random noise. In calculations, $P_s = (3/2)p^2$ and p is determined from (8), and $P_n = \sigma^2$ for both the real and imaginary components.

Results from applying the fixed beamformer to this complex distributed source of waves and noise show that for wide ranges of Δf and SNR values among the distributed sources, the general locations of these wave sources have been accurately deduced by this method.

A representative result of these tests is illustrated in Fig. 3c with SNR = 20 dB and $\Delta f = \pm 0.04\, f_A$ in f_B and f_C. This figure shows the divergence measure applied to the fixed beamformer maximum power source direction data. In Fig. 3c, the three source areas at {0,0}, {10,0}, and {7,10} are clearly identified. The results also show an additional source area at the geometric center of the three wave sources, where their waves collide. While this additional source area indicates where the three waves strongly interact it may also indicate new wave activities emerged from interferences of waves and noises from the three original sources. This notion that new wave activities–centers emerge from the interference of waves of strong convection in the tropical atmosphere requires further evaluation from observations. Although this test result indicates that the fixed beamformer can detect, in addition to the original wave sources, signals emerging from the interference of waves from the original sources, it further confirms the capacity of this fixed beamforming technique to deduce from noisy data the source regions of wave activities in a complex source environment.

b. *Applications of the fixed beamforming technique: Detecting source regions of tropical ISO*

After the fixed beamforming technique was evaluated and tested using the known wave sources of various complexities, it was applied to identify source regions of ISO in the tropical Indian and Pacific Oceans. Before discussing these applications we describe some details of the tropical ISO to provide a background necessary for the understanding of the fixed beamforming results. As originally described in Madden and Julian (1971, 1972), the intraseasonal time-scale oscillations in zonal wind, moisture, convection, and precipitation in the tropical Indian and western Pacific Ocean regions are groups of large-scale waves propagating eastward at a phase speed ~5 m s^{-1}. The frequency of the oscillations is rather broad, however, yielding a wide range of periods from 30 to 60 days (some even reported 90 days). Observations have found that the oscillations dissipate away from the western tropical Pacific in both zonal and meridional directions (Chang 1977; Hsu et al. 1990; Gustafson and Weare 2004a,b), indicating some sources of the oscillations confined in the tropical Indian and western Pacific region. The causes of these oscillations still remain unclear, albeit many possible mechanisms have been proposed and can explain certain features and aspects of the oscillations (e.g., Lau and Peng 1987; Neelin et al. 1987; Emanuel 1987; Chang and Lim 1988; Wang 1988; Blade and Hartmann 1993; Hu and Randall 1994, 1995; Woolnough et al. 2000; Raymond 2001; Stephens et al. 2004). It is expected that if we can identify the source regions of these ISO we may collect and examine the data within the source regions. From examining the source properties we may identify dynamic and thermodynamic processes initiating and nurturing the development of the intraseasonal oscillations. While understanding these oscillations we may also apply these processes in predictions of the oscillations and their effects on tropical weather and subtropical and midlatitude monsoons.

1) DATA

The data used in this application to detect tropical ISO with fixed beamforming were from the European Centre for Medium-Range Weather Forecasts (ECMWF) reanalysis dataset. We used 850-hPa zonal winds for the 29-yr period from 1974 to 2002 covering the globe with horizontal resolution of 2.5° × 2.5° in longitude and latitude. In addition, OLR data for the same 29 yr from the National Oceanic and Atmospheric Administration–Cooperative Institute for Research in Environmental Sciences (NOAA–CIRES) Climate Diagnostics Center (Liebmann and Smith 1996) were used.

Zonal winds at 850 hPa are used because low-level disturbances at 850 hPa often develop a few days before major convection in the intraseasonal oscillations when the upper troposphere is still showing subsidence and cooling (e.g., Hu and Randall 1994; Kiladis et al. 2005). Additionally, the zonal wind plays a dominant role in low-level convergence, whereas the meridional wind perturbations play a noticeable role only after the peak convection and when the westerly wind anomaly appears or strengthens (Houze et al. 2000; Tung and Yanai 2002). Thus, 850-hPa zonal wind is a relevant and informative variable to use in detecting the early development of convection and wave activities and, therefore, the source regions of ISO.

Some of these early wave activities may develop into full-scale supercloud clusters in ISO. As shown in Kiladis et al. (2005), in such development the atmospheric boundary layer is further destabilized to enhance fluxes of energy and water from the warm ocean surface to the atmosphere. Subsequently, convection intensifies in the entire troposphere by releasing latent heat and enhancing strong vertical motion in the upper troposphere. The deep convection can be described by very low OLR. Thus, OLR anomaly is another proper index to describe convection development and can be used in conjunction with 850-hPa zonal wind anomalies for applications of the fixed beamforming technique to identify the source regions of ISO.

There will be likely spatial as well as temporal differences between the ISO source regions identified by

OLR variations and by 850-hPa zonal wind fluctuations, however. These differences arise because of the vertical tilt of deep convection due to vertical shear of the zonal winds and vertical transport of horizontal momentum in deep convection. Moreover, the OLR is a parameter showing the outcome or consequence of the complex processes in the development of ISO whereas the 850-hPa zonal wind is one variable directly involved in these processes, particularly in their early stages of development. Some of the ISO signals in 850-hPa zonal wind may not develop into full-scale ISO before dissipating, thus being absent in the OLR variations. Nevertheless, because all the *developed* ISO shall have self-consistent anomalies in both the lower and upper troposphere averaged over their life cycles, ISO source regions in 850-hPa zonal winds shall have corresponding indications of such regions in deep convection and OLR.

Before the OLR and the zonal wind data were applied to the fixed beamformer, they were subjected to the Lanczos bandpass filter to isolate the variations (signals) in the intraseasonal frequencies. According to Duchon (1979), the minimum number of weights in the Lanczos filter, NC, is determined by $NC \geq 1.3(TCB - TCE)$, where TCE and TCB are the cutoff period in the high end and low end of the frequency spectrum, respectively. We used TCE = 30 days and TCB = 60 days in order to obtain a close to 1.0 response for the specified frequency band and also to reduce the edge effects on the filtered signals from the wings of the response function. With these considerations we obtained NC = 59. It is necessary to point out that although the filtered OLR and low-level wind data contain intraseasonal waves of a range of frequencies the source regions of these waves can be deduced by the fixed beamforming technique, as illustrated in its simulation with the complex distributed source in 3a.

2) ISO SOURCE REGIONS IDENTIFIED BY THE FIXED BEAMFORMER

From the large volume of daily data of the 29 yr (1974–2002) we first inspected annual time–longitude (Hovmöller) diagrams of filtered 850-hPa zonal winds averaged from 10°S to 10°N and from the tropical Indian to the tropical Pacific Ocean (from 40°E to 80°W), where the ISO is most prominent. This inspection helped identify the major ISO events. These events satisfy the criterion that there were at least two complete identifiable cycles of intraseasonal variations. We used this criterion because there were many individual cases in wind and OLR variations that appeared having some features of intraseasonal oscillation but only persisted for a period of 20–30 days, showing no oscillations. These cases were excluded from further analysis.

The selected ISO events satisfying the previous criterion occurred from 21 March to 31 May 1974, 28 September 1976 to 10 January 1977, 1 April to 31 May 1982, 1 January to 31 March 1988, and from 1 December 1991 to 10 February 1992, and 1 November 1994 to 31 January 1995. As an example, Figs. 4a and 4c show the time–longitude diagrams of 850-hPa zonal wind and OLR for the event from September 1976 to March 1977. The 850-hPa zonal wind and OLR anomalies in Figs. 4a and 4c have similar features. Centers of anomalies in the low-level wind and OLR propagated eastward after emerging in the tropical Indian Ocean. Additionally, the anomalies alternated, forming nearly two complete cycles of intraseasonal variation. Centers of peak anomalies in both 850-hPa wind and OLR in the Indian and western tropical Pacific Ocean suggest alternations of enhanced–weakened (or absence of) convection in those regions at intraseasonal time scales. Moreover, these regions were shown to be confined in the equatorial Indian and western Pacific Ocean region.

In detecting the source regions in this ISO event, we first estimated the wavelength of the ISO using the filtered time–longitude diagram of the 850-hPa zonal wind (Fig. 4a). Because phase speed and period of the oscillations can be more accurately estimated from the diagram, they were calculated and used to compute the wavelength from wavelength = phase speed × period. Albeit this estimation is not very accurate, this is the only way to determine the wavelength associated with the ISO. Using this method, we obtained the wavelength of 210° of longitude for this case. This wavelength suggests this case is a wavenumber 1 event. With this estimated wavelength the fixed beamforming technique was applied through the tropical region from 40°E to 80°W over the period of the observed life cycle of this event to detect the source regions of ISO. These detected source regions from the 850-hPa wind and OLR variations are shown in Figs. 4b and 4d, respectively.

Inspecting the ISO source regions shown in Figs. 4b and 4d, we also find similar patterns, a result supporting consistent features in both the wind and convection variations for these developed ISO events. Figure 4b shows an east–west belt of ISO source regions in the tropical Indian Ocean. There are also source regions over the Indonesian maritime region. In the western tropical Pacific, the sources are shown embedded in two split bands, one along the South Pacific Convergence Zone (SPCZ) and the other along the ITCZ north of the equator, and the latter is much weaker than the former (in northern winter). In accordance, the source regions detected in OLR in Fig. 4d show a single belt of sources in the tropical Indian Ocean and split bands of sources straddling the equator in the western and central tropical Pacific.

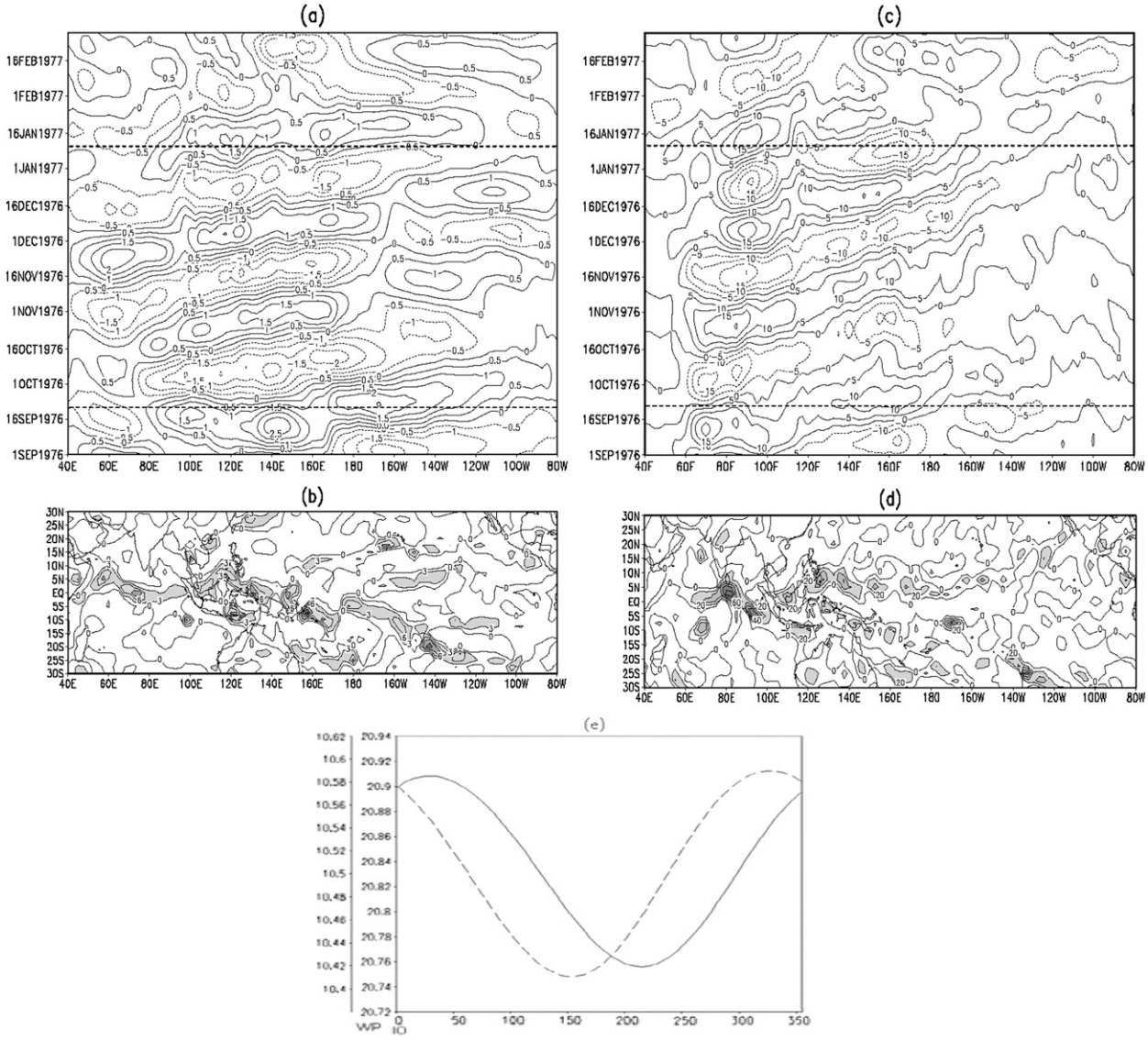

FIG. 4. Time–longitude diagram of 10°S–10°N averaged 30–60-day Lanczos bandpass-filtered (a) 850-hPa zonal wind anomalies (units: m s^{-1}, contour interval: 0.5) and (c) OLR anomalies (units: W m^{-2}, contour interval: 5.0). Negative anomalies are shown by dashed lines. The ISO event from 28 Sep 1976 to 10 Jan 1977 is marked by the two transverse dark dashed lines. ISO source regions deduced from (b) wind (units: 10^{-6} s^{-2}, contour interval: 3×10^{-6}, values $\geq 3 \times 10^{-6}$ s^{-2} are shaded) and (d) OLR (units: 10^{-6} W m^{-3}, contour interval: 20×10^{-6}, values $\geq 20 \times 10^{-6}$ W m^{-3} are shaded) by the fixed beamforming technique during 28 Sep 1976–10 Jan 1977. The positive values show emitting of the signals. Shaded regions show strength of emission larger than (b) 3×10^{-6} s^{-2} and larger than (d) 20×10^{-6} W m^{-3}. (e) The $p(\varphi)$ (units: m s^{-1}) distributions of ISO signal measured at two points: (2.5°N, 85°E) in the tropical Indian Ocean (solid line) and at (5.0°N, 145.0°E) in western tropical Pacific Ocean (long dashed line). Abscissa in (e) indicates the angle of arrival from 0° to 355° with a 5° increment. The two ordinates on the left show the magnitudes of $p(\varphi)$ at the Indian Ocean (IO) and the western tropical Pacific (WP) locations, respectively. The single peak in the two curves shows the unambiguous nature of the fixed beamformer in detecting the intraseasonal signal.

It is important to show that the power square root $p(\varphi)$ [see Eq. (8)] plotted in Fig. 4e from two sensor locations in the tropical Indian and western Pacific Ocean region has a single peak in the power of the detected signal. This indicates a unique direction from which the ISO waves are emanating. Thus, from these sensor locations a unique source of the ISO can be detected and identified. The same result also was found in many other sensor locations across the study region. This property demonstrates the ability of the fixed beamformer to *uniquely* detect the source regions of waves–signals in this application.

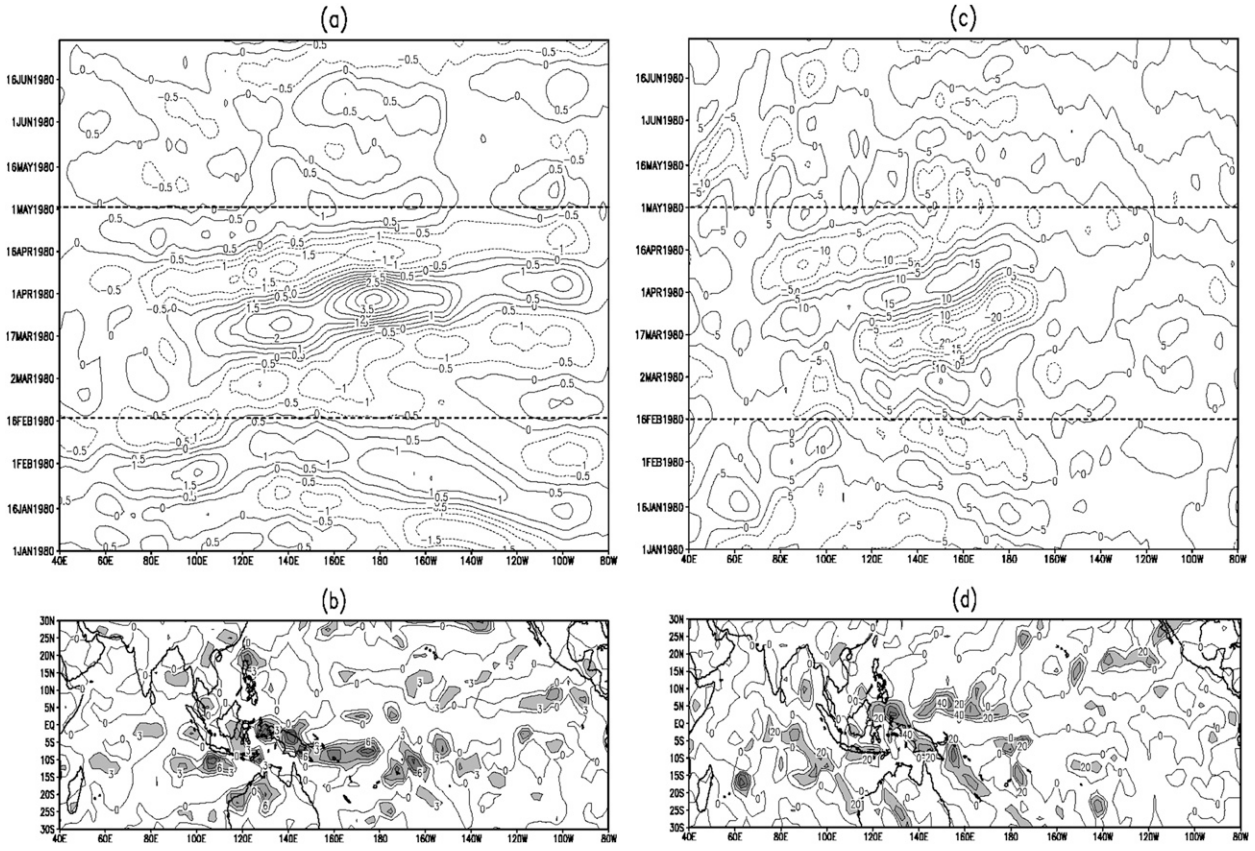

FIG. 5. Same as in Figs. 4(a)–(d), but for 16 Feb–30 Apr 1980 ISO event.

A major difference between these ISO sources detected from OLR and the 850-hPa zonal wind variations is the slight shift of some of the source region locations, although minor differences also are shown in intensities, particularly for the sources embedded in the SPCZ. These differences could have occurred because of the previously discussed differences in physical processes described by these two variables and the fact that the OLR describes upper-tropospheric anomalies and the 850-hPa zonal wind represents the lower-tropospheric anomalies during ISO. Except for these differences, the similar patterns in these results indicate consistent source regions of ISO in the tropical Indian and western Pacific Ocean region.

In addition to the events similar to the one shown in Fig. 4 there are events in which ISO only originated in the western tropical Pacific and propagated eastward. Two such events were identified: one is from 16 February to 30 April 1980 and the other from 6 August to 15 October 1996. For the former event, its time–longitude diagrams of the filtered 850-hPa zonal wind and OLR variations are shown in Figs. 5a and 5c, respectively, and their corresponding source regions of ISO detected by the fixed beamforming technique are shown in Figs. 5b and 5d.

In Figs. 5a and 5c the anomalies in both the 850-hPa wind and OLR originated in the Indonesian maritime region and west tropical Pacific Ocean, particularly in the first cycle of the event, and propagated eastward. In the second cycle, starting in April 1980, the anomalies were initiated in a rather different source region in the eastern tropical Indian Ocean and emanated eastward. The averaged wavelength of the two cycles is 160° longitude, close to being a wavenumber 1 event. These sources of the ISO packets are shown in Figs. 5b and 5d, strong in the western tropical Pacific region. Farther to the east, the ISO signal band splits into the ITCZ and the SPCZ, sustaining the eastward propagation of the intraseasonal variations in wind and OLR.

Five additional events of ISO occurred from 1974 to 2002: 11 February–20 May 1978, 1 July–30 September 1981, 21 September–30 November 1985, 1 March–31 May 1996, and 16 July–20 October 2000, respectively. These events share a feature of confined propagation; their entire life cycle was started and completed within the tropical Indian or the western equatorial Pacific

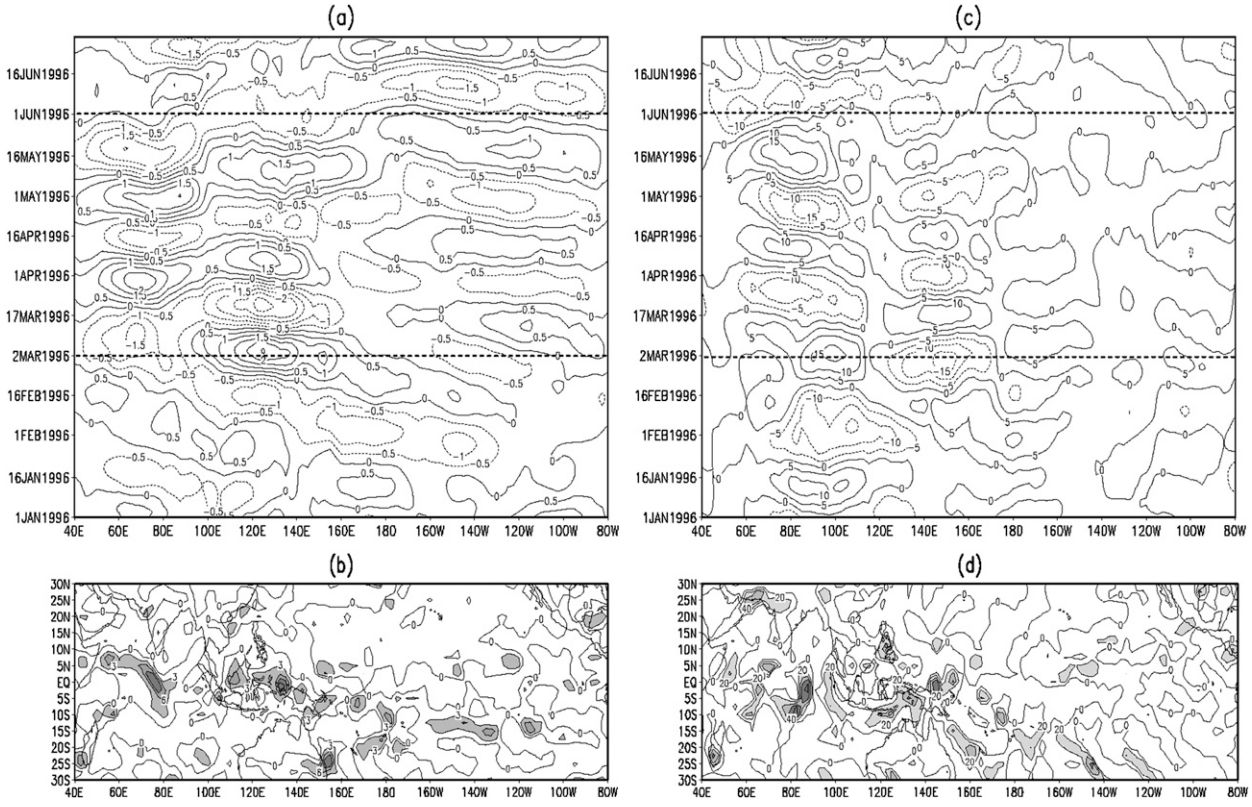

FIG. 6. Same as in Fig. 5, but for 1 Mar–31 May 1996 ISO event.

region. The event in 1996 is a good representation of these events, and its time–longitude diagram of filtered 850-hPa zonal wind and OLR variations and results from applications of the fixed beamforming technique are shown in Fig. 6.

In Fig. 6a, although intraseasonal variations in the 850-hPa zonal wind in the tropical Indian Ocean and western tropical Pacific region show some kind of connection, the northwest–southeast orientation of the axis of the major wind anomalies in the western tropical Pacific suggests its variations were rather different from that in the tropical Indian Ocean region. These differences indicate the presence of separate and local source regions that may have initiated and sustained such different ISO signals in the tropical Indian and western Pacific Ocean region.

These separate sources of ISO are detected by the fixed beamforming technique in both the low-level zonal wind and OLR, using an estimated wave span of 70° longitude, and shown in Figs. 6b and 6d. Major sources detected from the wind and OLR variations also are similar. Comparisons of these sources with the variations in the wind and OLR anomalies in Figs. 6a and 6c indicate correspondence of the ISO source regions to the centers of the intraseasonal variations in wind and OLR in the tropical Indian and west Pacific region.

4. Conclusions

A fixed beamforming technique is implemented on interpolated grids of atmospheric data to detect and identify the source regions of tropical ISO. Accurate detection of these source regions could help to understand initiation and predict development of these disturbances. After the method was successfully tested using both single and complex distributed simulated wave sources of known properties, it was applied to deduce the source regions of the tropical ISO, which have strong effects on Indian and Southeast Asian summer monsoons and precipitation in the western equatorial Pacific. Results of the fixed beamforming technique showed the various source regions of all major ISO events in the tropical Indian and western equatorial Pacific region during the 29 yr from 1974 to 2002. The significance of identifying these ISO source regions is that in knowing where the ISO was initiated and developed we can examine specific physical conditions and identify dynamic and thermodynamic

properties and processes in the development of these ISO. So far, investigations of the development of ISOs have been relying on large-scale averaged fields in the tropical atmosphere because of a lack of specific knowledge of ISO source regions. These average fields may have substantially weakened or even missed some processes specific for the development of ISO. This problem may be overcome by knowing the exact source regions of the ISO, where detailed information of dynamic and thermodynamic properties and structures can be extracted and analyzed. In addition, in these ISO source regions intraseasonal waves are generated and will further interact with their environment and result in rich behavior and spatial structures of the observed tropical convection and wind variations. As shown in Figs. 4–6, some of these interactions have led to continuous propagation of the ISO, while some other interactions have resulted in intraseasonal variations in convection that are primarily confined within the tropical Indian or the western equatorial Pacific region. From examining the details of these structures in the source regions we may gain additional understanding of the processes responsible for these different intraseasonal oscillation events.

Acknowledgments. We thank three anonymous reviewers and the editor for their comments and suggestions that led to improvement of this manuscript. This work was supported by the USDA Agricultural Research Project NEB-40-040.

REFERENCES

Blade, I., and D. L. Hartmann, 1993: Tropical intraseasonal oscillations in a simple nonlinear model. *J. Atmos. Sci.,* **50,** 2922–2939.

Chang, C. P., 1977: Viscous internal gravity waves and low-frequency oscillations in the tropics. *J. Atmos. Sci.,* **34,** 901–910.

——, and H. Lim, 1988: Kelvin wave-CISK: A possible mechanism for the 30–50 day oscillations. *J. Atmos. Sci.,* **45,** 1709–1720.

Cheong, B. L., M. W. Hoffman, R. D. Palmer, S. J. Frasier, and F. J. López-Dekker, 2004: Pulse pair beamforming and the effects of reflectivity field variations on imaging radars. *Radio Sci.,* **39,** RS3014, doi:10.1029/2002RS002843.

Duchon, C. E., 1979: Lanczos filtering in one and two dimensions. *J. Appl. Meteor.,* **18,** 1016–1022.

Emanuel, K. A., 1987: Air-sea interaction model of intraseasonal oscillations in the tropics. *J. Atmos. Sci.,* **44,** 2324–2340.

Gustafson, W. I., and B. C. Weare, 2004a: MM5 modeling of the Madden–Julian oscillation in the Indian and west Pacific Oceans: Model description and control run results. *J. Climate,* **17,** 1320–1337.

——, and ——, 2004b: MM5 modeling of the Madden–Julian oscillation in the Indian and west Pacific Oceans: Implications of 30–70-day boundary effects on MJO development. *J. Climate,* **17,** 1338–1351.

Houze, R. A., Jr., S. Y. Chen, D. E. Kinsmill, Y. Serra, and S. E. Yuter, 2000: Convection over the Pacific warm pool in relation to the atmospheric Kelvin–Rossby wave. *J. Atmos. Sci.,* **57,** 3058–3089.

Hsu, H. H., B. J. Hoskins, and F.-F. Jin, 1990: The 1985/86 intraseasonal oscillation and the role of the extratropics. *J. Atmos. Sci.,* **47,** 823–839.

Hu, Q., and D. A. Randall, 1994: Low-frequency oscillations in radiative–convective systems. *J. Atmos. Sci.,* **51,** 1089–1099.

——, and ——, 1995: Low-frequency oscillations in radiative–convective systems. Part II: An idealized model. *J. Atmos. Sci.,* **52,** 478–490.

Kiladis, G. N., K. H. Straub, and P. T. Haertel, 2005: Zonal and vertical structure of the Madden–Julian oscillation. *J. Atmos. Sci.,* **62,** 2790–2809.

Lacoss, R. T., 1968: Adaptive combining of wideband array data for optimal reception. *IEEE Trans. Geosci. Electron.,* **6,** 78–86.

Landsea, C. W., and W. M. Gray, 1992: The strong association between western Sahelian monsoon rainfall and intense Atlantic hurricanes. *J. Climate,* **5,** 435–453.

Lau, K. M., and P. H. Chen, 1986: Aspects of the 40-50 day oscillation during northern summer as inferred from outgoing longwave radiation. *Mon. Wea. Rev.,* **114,** 1354–1367.

——, and L. Peng, 1987: Origin of low-frequency (intraseasonal) oscillations in the tropical atmosphere. Part I: Basic theory. *J. Atmos. Sci.,* **44,** 950–972.

Liebmann, B., and C. A. Smith, 1996: Description of a complete outgoing longwave radiation dataset. *Bull. Amer. Meteor. Soc.,* **77,** 1275–1277.

Madden, R. A., and P. R. Julian, 1971: Detection of a 40–50 day oscillation in the zonal wind in the tropical Pacific. *J. Atmos. Sci.,* **28,** 702–708.

——, and ——, 1972: Description of global-scale circulation cells in the tropics with a 40–50 day period. *J. Atmos. Sci.,* **29,** 1109–1123.

Marple, S. L., Jr., 1999: Computing the discrete-time 'analytic' signal via the FFT. *IEEE Trans. Signal Process.,* **47,** 2600–2603.

Neelin, J. D., I. M. Held, and K. H. Cook, 1987: Evaporation-wind feedback and low-frequency variability in the tropical atmosphere. *J. Atmos. Sci.,* **44,** 2341–2348.

Raymond, D. J., 2001: A new model of the Madden–Julian oscillation. *J. Atmos. Sci.,* **58,** 2807–2819.

Stephens, G. L., P. J. Webster, R. H. Johnson, R. Engelen, and T. L'Ecuyer, 2004: Observational evidence for the mutual regulation of the tropical hydrological cycle and tropical sea surface temperatures. *J. Climate,* **17,** 2213–2224.

Tung, W. W., and M. Yanai, 2002: Convective momentum transport observed during the TOGA COARE IOP. Part I: General features. *J. Atmos. Sci.,* **59,** 1857–1871.

van Veen, B. D., and K. M. Buckley, 1988: Beamforming: A versatile approach to spatial filtering. *IEEE ASSP Mag.,* **5,** 4–24.

Wang, B., 1988: Dynamics of tropical low-frequency waves: An analysis of the moist Kelvin wave. *J. Atmos. Sci.,* **45,** 2051–2065.

——, and L. Ho, 2002: Rainy season of the Asian-Pacific summer monsoon. *J. Climate,* **15,** 386–398.

Wang, S., and F. Zhang, 2007: Sensitivity of mesoscale gravity waves to the baroclinicity of jet front systems. *Mon. Wea. Rev.,* **135,** 670–688.

Woolnough, S. J., J. M. Slingo, and B. J. Hoskins, 2000: The relationship between convection and sea surface temperature on intraseasonal time scales. *J. Climate,* **13,** 2086–2104.

Yasunari, T., 1979: Cloudiness fluctuations associated with the Northern Hemisphere summer monsoon. *J. Meteor. Soc. Japan,* **57,** 227–242.

Zhang, F., 2003: Effects of moist convection on mesoscale predictability. *J. Atmos. Sci.,* **60,** 1173–1185.